

Magma ascent mechanisms in the transition regime from solitary porosity waves to diapirism

Janik Dohmen¹, Harro Schmeling¹

¹Institute for Geoscience, Goethe University, Frankfurt, Germany

Correspondence to: dohmen@geophysik.uni-frankfurt.de

5 Abstract

In partially molten regions inside the earth melt buoyancy may trigger upwelling of both solid and fluid phases, i.e. diapirism. If the melt is allowed to move separately with respect to the matrix, melt perturbations may evolve into solitary porosity waves. While diapirs may form on a wide range of scales, porosity waves are restricted to sizes of a few times the compaction length. Thus, the size of a partially molten perturbation in terms of compaction length controls whether a diapir or a porosity wave is dominant. We study the transition from diapiric rise to solitary porosity waves by solving the two-phase flow equations of conservation of mass and momentum in 2D with porosity dependent matrix viscosity. We systematically vary the initial size of a porosity perturbation from 1.8 to 120 times the compaction length.

15 If the perturbation is of the order of a few compaction lengths, a single solitary wave will emerge, either with a positive or negative vertical matrix flux and if melt is not allowed to move separately to the matrix a diapir will emerge. In between these end members we observe a regime where the partially molten perturbation will split up into numerous solitary waves, whose phase velocity is so low compared to the Stokes velocity that the whole swarm of waves will ascend jointly as a diapir, just slowly elongating due to a higher amplitude main solitary wave.

20 Only if the melt is not allowed to move separately to the matrix no solitary waves will build up, but as soon as two-phase flow is enabled solitary waves will eventually emerge. The required time to build them up increases non-linearly with the perturbation radius in terms of compaction length and might be for many cases too long to allow for them in nature.

25 1 Introduction

In many scenarios inside the earth the process of a fluid moving relatively to a viscously deformable porous matrix is an important transport mechanism. The physics of these scenarios were firstly described by McKenzie (1984) and it was later shown by several authors that these equations allow for the emergence of solitary porosity waves (Scott & Stevenson, 1984; Barcilon & Lovera 1989; Wiggins & Spiegelman, 1995). Porosity waves are regions of localized excess fluid that ascend with permanent shape and constant velocity, controlled by compaction and decompaction of the surrounding matrix.

30 Porosity waves were of vast interest for many authors over the last decades and the possible consequences on geochemistry and fluid flow in lower and middle crust in general (e.g. Watson &

Spiegelman, 1994; McKenzie, 1984; Connolly, 1997; Connolly & Podladchikov, 2013, Jordan et al.,
35 2018, Richard et al., 2012) or the effects of matrix rheology on porosity waves (e.g. Connolly &
Podladchikov, 1998; Yarushina et al., 2015; Connolly & Podladchikov, 2015; Omlin et al., 2017;
Dohmen et al., 2019) have been examined. However, there are still open questions, regarding, for
example, that of the scaling. The size of a solitary porosity wave is usually of the order of a few
40 compaction lengths (McKenzie, 1984; Scott & Stevenson, 1984; Simpson & Spiegelman, 2011), but
this length scale varies over a few orders of magnitude, depending on the shear and bulk viscosity of the
matrix, fluid viscosity and permeability (see 1) with typical values of 100-10000 meters (McKenzie,
1984; Spiegelman, 1993).

On the other hand, partially molten regions in the lower crust or upper mantle are prone to gravitational
instabilities such as Rayleigh-Taylor instabilities or diapirism (e.g. Griffith, 1986; Bittner and
45 Schmeling, 1995; Schmeling et al., 2019). As characteristic wavelengths of Rayleigh-Taylor instabilities
may be similar, but also of significantly different order of those of porosity waves, the question arises
how these two mechanisms interact and how the transition between magmatic rise due to diapirism or
porosity wave look like. Scott (1988) already investigated a similar scenario. He calculated porosity
waves changing the compaction length by altering the constant shear to bulk viscosity ratio. In contrast,
50 we vary the radius of a partially molten perturbation in terms of compaction lengths but keeping the
porosity dependent viscosity law the same. While Scott (1988) was not able to reach the single-phase
flow endmember due to his setup, we can reach this endmember with our description and can explore
the transition.

The extent of partially molten scenarios inside the earth's mantle vary over many orders of magnitude
55 and this transition might have an important effect on the evolution of these regions. In this work we
want to address this problem and look especially on what happens for different sizes of initial
perturbations and what are the numerical implications on modelling magma transport.

Addressing different melt ascent mechanisms, it may be useful to specify our definition of diapirism.
Originating from the Greek "*diapirein*", i.e. "to pierce through", diapirism describes the "buoyant
60 upwelling of relatively light rock" (Turcotte & Schubert, 1982) through and into a denser overburden.
In the general definition the rheology of the diapir and ambient material is not specified, both can be
ductile as in our case, but often, the overburden is assumed being more viscous or even brittle. Buoyancy
may be of compositional or phase related origin, e.g. due to the presence of non-segregating partial melt
(Wilson, 1989). Based on these definitions in our case a diapir is a rising, partially molten body or
65 porosity anomaly with zero fluid-solid separation velocity. Mathematically the equations of motion of
the two-phase system degenerate to the Stokes equation (see below).

2 Theoretical Approach

2.1 Governing equations

The formulation of the governing equations for the melt-in-solid two-phase flow dynamics is based on McKenzie (1984), Spiegelman & McKenzie (1987) and Schmeling (2000) assuming an infinite Prandtl number, a low fluid viscosity w.r.t. the effective matrix viscosity, zero surface tension, and the Boussinesq approximation. In the present formulation the Boussinesq approximation assumes the same constant density for the solid and fluid except for the buoyancy terms of the momentum equations for the solid and fluid. In the following all variables associated with the fluid (melt) have the subscript f and those associated with the solid have the subscript s . Applying the Boussinesq approximation the equation for the conservation of the mass of the melt is

$$\frac{\partial \varphi}{\partial t} + \vec{\nabla} \cdot (\varphi \vec{v}_f) = 0, \quad (1)$$

and the mass conservation of the solid is

$$\frac{\partial(1-\varphi)}{\partial t} + \vec{\nabla} \cdot ((1-\varphi)\vec{v}_s) = 0. \quad (2)$$

φ is the volumetric rock porosity (often called melt fraction), \vec{v}_f and \vec{v}_s are the fluid and solid velocities, respectively. The momentum equations are given as a generalized Darcy equation for the fluid separation flow

$$\vec{v}_f - \vec{v}_s = -\frac{k_\varphi}{\eta_f \varphi} (\vec{\nabla} P - \rho_f \vec{g}), \quad (3)$$

where ρ_f is the fluid density and P is the fluid pressure (including the lithostatic pressure), whose gradient is driving the motion. The Stokes equation for the mixture is given as

$$\rho \vec{g} - \vec{\nabla} P + \frac{\partial \tau_{ij}}{\partial x_j} = 0. \quad (4)$$

k_φ is the permeability that depends on the rock porosity

$$k_\varphi = k_0 \varphi^n, \quad (5)$$

η_f is the melt dynamic viscosity, \vec{g} is the gravitational acceleration, ρ is the density of the melt – solid mixture and τ_{ij} is the viscous stress tensor

$$\tau_{ij} = \eta_s \left(\frac{\partial v_{si}}{\partial x_j} + \frac{\partial v_{sj}}{\partial x_i} \right) + \left(\eta_b - \frac{2}{3} \eta_s \right) \delta_{ij} \nabla \cdot \vec{v}_s. \quad (6)$$

η_b is the bulk viscosity. The linearized equation of state for the mixture density is given as

$$\rho = \rho_0 (1 - c_f \varphi) \quad (7)$$

with ρ_0 as the solid density and $c_f = \frac{\rho_0 - \rho_f}{\rho_0}$. The shear and bulk viscosity are given by the simple equations

$$\eta_s = \eta_{s0}(1 - \varphi) \quad (8)$$

and

$$\eta_b = \eta_{s0} \frac{1-\varphi}{\varphi} \quad (9)$$

where η_{s0} is the constant intrinsic shear viscosity of the matrix.

100 As in both equations (3) and (4) P is the fluid pressure (see McKenzie, 1984, Appendix A), these equations can be merged to eliminate the pressure resulting in

$$\vec{v}_f - \vec{v}_s = -\frac{k_0 \varphi^{n-1}}{\eta_f} \left(\rho_0 c_f \vec{g}(1 - \varphi) + \frac{\partial \tau_{ij}}{\partial x_j} \right). \quad (10)$$

This equation states that the fluid separation flow (i.e. melt segregation velocity) is driven by the buoyancy of the fluid with respect to the solid and the viscous stress in the matrix including compaction and decompaction.
105

Following Šrámek *et al.* (2010), the Stokes equation (3) can be rewritten by expressing the matrix velocity, \vec{v}_s , as the sum of the incompressible flow velocity, \vec{v}_1 , and the irrotational (compaction) flow velocity, \vec{v}_2 , as:

$$\vec{v}_s = \vec{v}_1 + \vec{v}_2 = \begin{pmatrix} \frac{\partial \psi}{\partial z} \\ -\frac{\partial \psi}{\partial x} \end{pmatrix} + \begin{pmatrix} \frac{\partial \chi}{\partial x} \\ \frac{\partial \chi}{\partial z} \end{pmatrix} \quad (11)$$

110 with ψ as stream function and χ as the irrotational velocity potential, given as the solution of the Poisson equation

$$\vec{\nabla}^2 \chi = \vec{\nabla} \cdot \vec{v}_s. \quad (12)$$

The divergence term $\vec{\nabla} \cdot \vec{v}_s$ can be derived from eqs. 1 and 2 to give

$$\vec{\nabla} \cdot \vec{v}_s = -\vec{\nabla} \cdot [\varphi(\vec{v}_f - \vec{v}_s)]. \quad (13)$$

115 In the small fluid viscosity limit the viscous stresses within the fluid phase are neglected, resulting in a viscous stress tensor in the Stokes equation of the mixture (equ. 4), in which only the stresses in the solid phase are relevant. This is evident from the definition of the viscous stress tensor, which only contains matrix and not fluid viscosities. Melt viscosities of carbonatitic, basaltic or silicic wet or dry melts span a range from < 1 Pa s to extreme values up to 10^{14} Pa s (see the discussion in Schmeling *et al.*, 2019), while effective viscosities of mafic or silicic partially molten rocks may range between 10^{20} Pa s and 10^{16} Pa s, depending on melt fraction, stress, and composition. Thus, in most circumstances the small fluid viscosity limit is justified.
120

In the limit of this small viscosity assumption, inserting the above solid velocity (11) into the viscous stress (6), this into the Stokes equation (4), and taking the curl of the x- and z equations the pressure is
 125 eliminated and one gets

$$\left(\frac{\partial^2}{\partial x^2} - \frac{\partial^2}{\partial z^2}\right) \left[\eta_s \left(\frac{\partial^2 \psi}{\partial x^2} - \frac{\partial^2 \psi}{\partial z^2} \right) \right] + 4 \frac{\partial^2}{\partial x \partial z} \left[\eta_s \frac{\partial^2 \psi}{\partial x \partial z} \right] = -g \frac{\partial \rho}{\partial x} + A(\chi) \quad (14)$$

with

$$A(\chi) = -2 \frac{\partial^2}{\partial x \partial z} \left[\eta_s \left(\frac{\partial^2 \chi}{\partial x^2} - \frac{\partial^2 \chi}{\partial z^2} \right) \right] + 2 \left(\frac{\partial^2}{\partial x^2} - \frac{\partial^2}{\partial z^2} \right) \left[\eta_s \frac{\partial^2 \chi}{\partial x \partial z} \right] \quad (14a)$$

To describe the transition from solitary waves to diapirs it is useful to non-dimensionalize the
 130 equations. As scaling quantities we use the radius r of the anomaly, the reference viscosity η_0 , and the scaling Stokes sphere velocity (e.g. Turcotte & Schubert, 1982) based on the maximum porosity of the anomaly φ_{max}

$$v_{St} = C_{St} \frac{\varphi_{max} \Delta \rho g r^2}{\eta_0} \quad (15)$$

resulting to the following non-dimensionalization where non-dimensional quantities are primed:

$$135 \quad (x, z) = (x', z') \cdot r, \quad \vec{v}_{s,f} = \vec{v}'_{s,f} \cdot v_{St}, \quad t = t' \cdot \frac{r}{v_{St}}, \quad (\tau_{ij}, P) = (\tau'_{ij}, P') \cdot \frac{\eta_0 v_{St}}{r},$$

$$(\eta_s, \eta_b) = (\eta'_s, \eta'_b) \cdot \eta_0, \quad (\psi, \chi) = (\psi', \chi') \cdot r v_{St} \quad (16)$$

For r the half width of the prescribed initial perturbation, consisting of a 2D Gaussian bell, is chosen. This is reasonable as the rising velocity in our code is best described by the Stokes velocity, using this radius. The exact shape of the perturbation is given later in the model setup.

140 C_{St} is calculated by using the analytic solution of an infinite Stokes cylinder within another cylinder (Popov and Sobolev (2008), based on the drag force derived by Slezkin (1955)), because, due to boundary effects, the cylinder gets effectively slowed. C_{St} is calculated using $C_{St} = \ln(k) - \frac{k^2-1}{k^2+1}$, where k is the ratio of outer cylinder's to inner cylinder's radius. For our model setup C_{St} is equal to 0.17.

145 With these rules the Darcy equation (10) is given in non-dimensional form

$$\vec{v}'_f - \vec{v}'_s = -\frac{\delta_c^2}{r^2} \frac{1}{\tilde{\eta}' \varphi} \left(\vec{e}_z \frac{(1-\varphi)}{\varphi_{max}} + \frac{\partial \tau'_{ij}}{\partial x'_j} \right) \quad (17)$$

where \vec{e}_z is the unit vector in z-direction and $\tilde{\eta}'$ is equal to $\eta'_b + \frac{4}{3} \eta'_s$, which is occasionally referred to as compaction viscosity. The momentum equation of the mixture (12) is given by

$$\left(\frac{\partial^2}{\partial x'^2} - \frac{\partial^2}{\partial z'^2}\right) \left[\eta'_s \left(\frac{\partial^2 \psi'}{\partial x'^2} - \frac{\partial^2 \psi'}{\partial z'^2} \right) \right] + 4 \frac{\partial^2}{\partial x' \partial z'} \left[\eta'_s \frac{\partial^2 \psi'}{\partial x' \partial z'} \right] = \frac{1}{\varphi_{max}} \frac{\partial \varphi}{\partial x'} + A'(\chi'). \quad (18)$$

150 δ_c^2/r^2 in equation (17) is the squared ratio of compaction length δ_c to the system length scale r , which is the main parameter describing our system. The compaction length is a typical length scale used in two-phase flow problems and of particular importance in our context, because 2D porosity waves have half width radii of the order of $3 \cdot \delta_c$ to $5 \cdot \delta_c$ (Simpson and Spiegelman, 2011). It is defined as:

$$\delta_c = \sqrt{\frac{\eta_b + \frac{4}{3}\eta_s}{\eta_f} k_\varphi} \quad (19)$$

155 In the other equations (1), (2), (6), (11), (12), (13), and (14a) all quantities are simply replaced by their non-dimensional primed equivalents.

We now can compare the two limits, where segregation or two-phase flow dominates (solitary wave regime), and where fluid and solid rise together with the same velocity as partially molten bodies (batch melting), which we identify with the diapir regime. This can be done by comparing the characteristic segregation velocity within solitary waves, which scales as

$$v_{sgr} \approx \frac{k_0 \varphi_{max}^{n-1}}{\eta_f} \left(\Delta \rho g (1 - \varphi_{max}) - \frac{\partial \tau_{ij}}{\partial x_j} \right) = C_{sgr} \frac{k_0 \varphi_{max}^{n-1} \Delta \rho g (1 - \varphi_{max})}{\eta_f} \quad (20)$$

where C_{sgr} is of the order $1/2$ for 2D solitary waves (Schmeling, 2000), with the characteristic Stokes sphere rising velocity given by (15). The ratio of these is given by

$$\frac{v_{sgr}}{v_{st}} = \frac{C_{sgr}}{C_{st}} \frac{r^2 \varphi_{max}^{n-2} (1 - \varphi_{max})}{\delta_c^2 \widetilde{\eta}'_0 \varphi_0^n} \quad (21)$$

165 Here $\widetilde{\eta}'_0$ refers to $\widetilde{\eta}'$ for the background porosity φ_0 . In contrast to Scott (1988), who varies the compaction viscosity in his model series, we vary the ratio of initial Stokes radius to compaction length.

Thus, *in the solitary wave limit*

$$\frac{C_{sgr}}{C_{st}} \frac{r^2 \varphi_{max}^{n-2} (1 - \varphi_{max})}{\delta_c^2 \widetilde{\eta}'_0 \varphi_0^n} \gg 1 \quad (22)$$

170 Darcy's law (17) results in large segregation velocity, which scales as

$$v_{sgr}' = \frac{C_{sgr}}{C_{st}} \frac{r^2 \varphi_{max}^{n-2} (1 - \varphi_{max})}{\delta_c^2 \widetilde{\eta}'_0 \varphi_0^n} \quad (23)$$

From equation (13) it follows that the irrotational part of the matrix velocity scales with

$$v_1 \approx -\varphi_{max} v_{sgr} \quad (24)$$

while the rotational part is given by (18): In that equation A' scales with χ' , which, via equ (12) and
 175 (13), scale with v_{sgr} , i.e. with $\frac{r^2}{\delta_c^2}$. In other words, the second term on the RHS of (18) dominates for
 small $\frac{\delta_c^2}{r^2}$ as the first term is of the order 1. Thus, the rotational matrix velocity has the same order as the
 irrotational compaction velocity and serves to accommodate the compaction flow. In this limit the
 buoyancy term in equation (18), $\frac{1}{\varphi_{max}} \frac{\partial \varphi}{\partial x'}$, is of vanishing importance for the matrix velocity and the
 matrix velocity, $\vec{v}_1 + \vec{v}_2$, is of the order of $\varphi_{max} v_{sgr}$. In the small porosity limit, matrix velocities are
 180 negligible with respect to fluid velocities.

In the diapir limit,

$$\frac{c_{sgr}}{c_{st}} \frac{r^2}{\delta_c^2} \frac{\varphi_{max}^{n-2} (1-\varphi_{max})}{\tilde{\eta}_0' \varphi_0^n} \ll 1 \quad (25)$$

and equation (17) predict vanishing segregation velocities. As A' and χ' scale with $\frac{r^2}{\delta_c^2}$, both vanish in
 the diapir limit, no irrotational matrix velocity occurs and equ. (18) reduces to the classical biharmonic
 185 equation (i.e. Stokes equation) driven by melt buoyancy and describing classical diapiric ascent.
 Segregation velocities are negligible with respect to matrix velocities.

In Fig. 1 the results of this simple analysis are shown, where we calculated the velocity ratios as a
 function of initial perturbation radius for several perturbation radii. In our models we use a φ_{max} of
 2%, for which we get a switch from solitary wave to diapir dominant behavior at $r = 48 \cdot \delta_c$. For bigger
 190 amplitudes this switch happens at a bigger radius and for smaller amplitudes the other way around.

2.2 Model setup

The model consists of a $L' \times L'$ box with a background porosity, φ_0 , of 0.5%. L' is the non-dimensional
 side length of the box and equal to 6 times the initial radius of the perturbation. As initial condition a
 non-dimensional Gaussian wave porosity anomaly is placed in the middle of the model at $x'_0 = 3$ and
 195 $z'_0 = 3$. The Gaussian wave is given by

$$\varphi = \varphi_{max} \cdot \exp\left(-\left(\frac{x'-x'_0}{w'}\right)^2 - \left(\frac{z'-z'_0}{w'}\right)^2\right) \quad (26)$$

Where φ_{max} is the amplitude equal to 0.02 in our models and w' corresponds to the width where φ has
 reached φ_{max}/e . In our case w' is equal to 1.2.

In our model series we vary the ratio of Stokes radius to compaction length from 1.8 to 48 to explore
 200 the parameter range towards the diapiric regime. The resolution of the models is chosen to be at least
 201×201 and was increased for higher length scale ratios so that the compaction length is resolved by
 at least 3-4 grid points.

At the top and the bottom, we prescribe an out- and inflow for both melt and solid, respectively, which is calculated analytically for the background porosity. This is necessary because we have a background melt fraction φ_0 that would lead to melt accumulation at the top of the model. We therefore calculate the segregation velocity of the background porosity φ_0 using equation (17) without the viscous stress term. The corresponding matrix velocity is calculated using the conservation of mass.

At the sides we use mirroring boundary conditions, which corresponds to a symmetry axis, where no horizontal flow is allowed. The permeability-porosity relation exponent in our models is always $n = 3$. To run models for a longer, practically infinite, amount of time we let the models coordinate system follow the maximum melt fraction. This is done by shifting the whole model down one grid length after φ_{max} has risen above $\frac{L'}{2} + dz$. This procedure allows us to zoom into the perturbation and follow it, not knowing its velocity and without carrying out any interpolations, which would strongly influence the model.

215

2.3 Numerical approach

The above equations in non-dimensional form are solved by the finite differences code FDCON developed essentially by one of the authors (Schmeling et al., 2019). Starting from the prescribed initial condition for φ , and assuming $A'(\chi') = 0$ at time 0, the time loop is entered and the biharmonic equation (19) is solved for ψ' by Cholesky decomposition, from which \vec{v}_1' is derived. Together with \vec{v}_2' the resulting solid velocity is used to determine the viscous stress term in the segregation velocity equation (17). This equation and the melt mass equation (1) are solved iteratively with strong underrelaxation for φ and $\vec{v}_f' - \vec{v}_s'$ for the new time step using upwind and an implicit formulation of equ. (1). During this internal iteration these quantities are used, via equ. (13), to give $\vec{\nabla} \cdot \vec{v}_s$, the divergence of the matrix velocity, which is needed in the viscous stress term (equ. 6). After convergence $\vec{\nabla} \cdot \vec{v}_s$ is used via equ. (12) to determine χ by LU-decomposition and then to get \vec{v}_2' . Now $A'(\chi')$ can be determined to be used on the RHS of equ (18). The procedure is then repeated upon entering the next time step.

Time steps are dynamically adjusted by the Courant criterion times 0.2 based on the fastest velocity, either melt or solid.

The model resolution is a critical parameter in this kind of numerical calculations and should always be kept in mind. With increasing length scale ratio, the compaction length in the model gets smaller and the resolution needs to be increased to keep it equally resolved.

According to several authors (e.g. Räss et al., 2019; Keller et al., 2013), the compaction length should be at least resolved by 4-8 grid points to solve for waves sufficiently accurately. For small length scale ratios this is no problem, where, with a model resolution of 201×201 , up to nearly 30 grid points per

235

compaction length can be achieved. The highest resolution our code can run is 601×601 , which is enough to resolve the compaction length by three grid points for the model with a length scale ratio of 48. Everything above that cannot be sufficiently resolved with respect to studying solitary waves.

240 Fig. 2 shows the resulting models for a length scale ratio of 12 for six different resolutions. The pictures were taken after φ_{max} has risen approximately 0.25 times the initial Stokes radius ($t' = 0.25$). With increasing resolution, the maximum melt fraction increases strongly from 101×101 to 401×401 by approximately 20% but the velocity of φ_{max} decreases by 7% (not shown in the figure). Both values converge. Even though the compaction length is not sufficiently resolved in Fig. 2d, one can still observe the main features of the model: A main solitary wave has emerged from the original gaussian
245 perturbation and secondary porosity waves are beginning to emerge within its wake. Even with $\delta_c/dx = 1$ these features can be observed but are much worse emphasized. With even lower resolutions accumulations at the top of the perturbation can be seen, which can be broadly interpreted as the attempt of a solitary wave to build up. With $\delta_c/dx = 0.24$, the model is too coarse and the results cannot be trusted anymore.

250 The solitary waves modeled with our code have been compared to the semi-analytical solution of Simpson & Spiegelman (2011), and more benchmarking was carried out in Dohmen et al. (2019).

In a single-phase flow case, where the melt is not allowed to move relatively to the solid, the initial perturbation ascends, shortly after beginning, with a velocity of 0.95 times the calculated Stokes velocity, and then slowly decreases as the original Gauss-shaped wave deforms and loses in amplitude.

255 **3 Results**

3.1 The transition from porosity wave to diapirism: Varying the initial wave radius

In this model series we vary the initial wave radius to cover the transition from porosity waves towards diapirism. As a reminder, due to our scaling the initial wave has always the same size w.r.t. the model box, and “increasing the initial wave radius” is equivalent to decreasing the compaction length or the
260 size of the emerging solitary waves w.r.t. the model box. In Fig. 3 the models are shown at $t' = 0.2$. For small radii ($r \leq 12 \cdot \delta_c$) a single porosity wave emerges from the original perturbation. The melt that is not situated within the emerging wave is left behind and has, for the most part, already left the model region. For $r = 2.4 \cdot \delta_c$ the emerged solitary wave is about the size of the initial perturbation and even smaller radii would lead to too big waves that would not fit into the model. With increasing radius, the
265 emerging solitary wave gets smaller. With $r = 12 \cdot \delta_c$, the resulting wave has just a size of $\sim 20\%$ the initial perturbation size.

We can compare the observed rising velocities of these solitary waves of Fig. 3b-e with hypothetical Stokes velocities of an equivalent diapir based on equation (15). While the dimensional Stokes velocity of a porosity anomaly is proportional to the amplitude of porosity and the square of the radius, the non-

270 dimensional Stokes velocity is always equal to 1. In Fig. 4 this non-dimensional Stokes velocity is indicated by the dashed line with the value 1. The colored lines give 2D solitary wave velocities with their appropriate radii, given by Simpson & Spiegelman (2011), normalized by the Stokes velocity corresponding to different initial perturbation radii. These semi analytical solutions fit quite nicely to our solitary wave models, as already shown in Dohmen et al. (2019). The velocities in this figure can be understood as ratios of solitary wave velocity to initial perturbation Stokes velocity. Inspection of Fig. 4 reveals that for the first four cases of Fig. 3b-e with radii smaller or equal $12 \cdot \delta_c$ the phase velocities are always larger than the Stokes velocity. For example, for $r = 12 \cdot \delta_c$, an emerging solitary wave with a typical radius of $4.5 \cdot \delta_c$ has a higher phase velocity than a $r = 12 \cdot \delta_c$ melt anomaly rising by Stokes flow. Thus, the cases are always in the solitary wave regime.

280 For greater radii (e.g. $r = 18 \cdot \delta_c - 30 \cdot \delta_c$, Fig. 3e-g) the phase velocities of solitary waves are of the order of the Stokes velocity (see Fig. 4) and they therefore need more time to separate from the remaining melt of the initial perturbation, still rising with order of Stokes velocity. The amount of melt accommodated within the main solitary wave is just a small percentage of the original perturbation and secondary waves can evolve in its remains. With further ascending, more and more solitary waves build up and the former perturbation will sooner or later consist of solitary waves in an ordered cluster or a formation. This formation elongates during ascend as the main wave has a larger amplitude than all the following waves, whose amplitudes are also decreasing with depth, as a higher proportion of melt accumulated at the top of the perturbation. Similar formations of strongly elongated fingers can be also observed in 3D as shown by Räss et al. (2019) who used decompaction weakening. In the models with smaller radii, the main solitary wave consisted of the majority of melt originally situated within the perturbation and the emergence of secondary waves turns out zero or small, but with greater radii enough melt is left behind to observe the emergence of second and higher generations of solitary waves.

290 For greater radii (e.g. $r = 24 \cdot \delta_c - 48 \cdot \delta_c$, Fig. 3f-j) the phase velocities of solitary waves are almost equal to the Stokes velocity (See Fig. 4). This leads to almost no separation after $t' = 0.2$. While for $r = 36 \cdot \delta_c$ a solitary wave has already build up and is rising just ahead of the perturbation, for $r = 42 \cdot \delta_c$ and $r = 48 \cdot \delta_c$ just the accumulation of melt at the top of the perturbation can be observed, which will eventually lead to a solitary wave. Secondary waves also build up with higher runtimes, as can be already seen for $r = 36 \cdot \delta_c$.

300 For even greater radii the compaction length cannot be sufficiently resolved with our approach, but tests with not sufficiently resolved models have shown that solitary waves can be observed for $r \geq 48 \cdot \delta_c$. At some point they do no longer appear, probably due to lack of sufficient resolution, but our tests show that solitary waves should always emerge, even if its phase velocity is way below the Stokes velocity. As long as the ascending time is long enough and melt is able to move separately to the matrix, independently of segregation velocity, a diapir will evolve into a swarm of a certain number of solitary waves, based on the compaction length. Because the phase velocities of each small solitary wave is

small compared to the Stokes velocity of the full swarm we consider such a rising formation of melt as a large scale diapir.

Fig. 3l shows the required time for the initial perturbation to build up a solitary wave. This status is achieved after the dispersion relation of the main wave reaches a point from where it follows the solitary wave dispersion relation. This time increases nearly linearly for small radii ($r \leq 48 \cdot \delta_c$) but increases non-linearly for greater radii. This might be due to lack of proper resolution, but a non-linear trend can be already observed for small radii. The transition time for radii smaller than $30 \cdot \delta_c$ is smaller than 0.2, the time at which the models in Fig. 3b-j are shown. The other models already show solitary wave like blobs but did not yet reach their final form.

Just in the case where the compaction length is zero ($r = \infty \cdot \delta_c$), i.e. melt is not able to move w.r.t. the matrix, a classical diapir, as shown in Fig. 3k, will evolve. Here, no focusing into solitary waves can be observed and the transition time is infinity.

Summarizing Fig. 4, the comparison of Stokes and porosity wave velocities correlates nicely with our observations shown in Fig. 3: For small initial radii the solitary wave velocity is clearly higher and will therefore build up and separate from the melt left behind quickly. With increasing radius, the velocity ratio decreases, and the waves need more time to build up and separate. But even with velocity ratios smaller than 1, solitary waves emerge and, not able to separate, rise just ahead of the remains, slowly elongating the initial perturbation.

3.2 Effects on the mass flux

It is important to study the partitioning between rising melt and solid mass fluxes in partially molten magmatic systems because melts and solids are carriers of different chemical components. Within our Boussinesq approximation we may neglect the density differences between solid and melt. Then our models allow to evaluate vertical mass fluxes of solid or fluid by depicting the vertical velocity components multiplied with the melt or solid fractions, respectively:

$$\begin{aligned} q'_{sz} &= (1 - \varphi) \cdot v'_{sz} \\ q'_{fz} &= \varphi \cdot v'_{fz}. \end{aligned} \tag{29}$$

Fig. 5 shows horizontal profiles through rising melt bodies at the vertical positions of maximum melt fraction at timesteps where the main wave has just reached the status of a solitary wave.

The mass fluxes of solid and fluid are strongly affected by the change of the initial radius from the solitary wave regime towards the diapiric regime. For $r = 2.4 \cdot \delta_c$, where we observe a solitary wave, the fluid has its peak mass flux in the middle of the wave and the solid is going downwards, against the phase velocity. In the center the fluid flux is about 10 times higher than the solid net flux. The upward flow in the center is balanced by the matrix dominated downward flow inside and outside the wave. For $r = 12 \cdot \delta_c$ the wave area is much smaller and the ratio between solid and fluid flux is still around the

order of 10. At the boundary of the wave the solid is nearly not moving at all, but a minimum can be observed within the center of it. For $r' = 24 \cdot \delta_c$ the solid flux is just above zero in the center and increases to a maximum towards the flanks of the wave, that is still about ten times smaller than the maximum fluid flux.

With $r' = 48 \cdot \delta_c$ the solid flux is just about three times smaller than the fluid flux, but most of the material ascend is accomplished by the solid. This suggests that diapiric rise begins to dominate.

So far, we have based our discussion of the transition from solitary waves towards diapirism on qualitative model observations. We now try to invoke a more quantitative criterion. In a horizontal line passing through the anomalies porosity maximum we define the total vertical mass flux of the rising magma body by $\int_{\varphi > \varphi_0} (q_f + q_s) dx$ where the integration is carried out only in the region of increased porosity $\varphi > \varphi_0$. This mass flux is partitioned between the fluid mass flux, $\int_{\varphi > \varphi_0} q_f dx$, and the solid mass flux, $\int_{\varphi > \varphi_0} q_s dx$. With these we define the partition coefficients

$$C_{soli} = \frac{\int_{\varphi > \varphi_0} q_f dx}{\int_{\varphi > \varphi_0} (q_f + q_s) dx} \quad (30)$$

and

$$C_{dia} = \frac{\int_{\varphi > \varphi_0} q_s dx}{\int_{\varphi > \varphi_0} (q_f + q_s) dx} \quad (31)$$

The sum $C_{soli} + C_{dia}$ is always 1 and if $C_{soli} > C_{dia}$ then the solitary wave proportion is dominant, while for $C_{soli} < C_{dia}$ diapirism is dominant. In Fig. 6a these partition coefficients for several initial radii are shown. In red are the diapir and in blue the solitary wave partition coefficients.

For $r = 1.8 \cdot \delta_c$, C_{soli} is equal to 5 and C_{dia} is equal to -4, i.e. we have a downward solid flux. With increasing radius C_{dia} increases until it changes its direction at $r \approx 20 \cdot \delta_c$, eventually becomes bigger than C_{soli} at $r = 36 \cdot \delta_c$ and then approaches 1 for bigger radii. C_{soli} changes so that the sum of both is always equal to 1. Even though diapirism is dominant for $r > 36 \cdot \delta_c$, we still observe solitary waves, yet their phase velocities are much smaller than the large scale rising velocities of the full melt formation.

In Fig. 6b the ratio of maximum fluid velocity (i.e. \vec{v}_f) to absolute matrix velocity is shown. For small radii, where $C_{soli} \gg C_{dia}$, this ratio is approximately constant with a high value of about 100. The absolute velocity maxima itself are not constant but decrease with the same rate until the switch of negative to positive matrix mass flux, where the absolute matrix velocity starts to increase, while the fluid velocity keeps decreasing. At this zero crossing we would expect a ratio of infinity, but while the zero crossing takes place within the center of the solitary wave, other regions near the wave still have finite vertical velocities. This switch from negative to positive mass flux was already observed by Scott

(1988), but while he changed the viscosity ratio as an independent constant model parameter, we change the radius and keep the viscosity law the same, still evolving with φ . Both describe the transition from a two-phase limit towards the Stokes limit, but in our formulation, we are able to reach the Stokes limit while Scott (1988) is still in the two-phase flow regime. With even greater radii the velocity ratio will eventually converge towards 1, where melt is no longer able to move relatively to the matrix (i.e. $\vec{v}_f = \vec{v}_s$) and material will be transported by a single phase. These last models are not sufficiently resolved to obtain leading and secondary solitary waves, but still show the expected behavior in terms of macroscopically rising partially molten diapir.

Based on these observations, the evolution of these models can be divided into two regimes: (1) In the solitary wave regime ($r \leq 36 \cdot \delta_c$) C_{solid} is larger than C_{dia} and the initial perturbation emerges into waves that have the properties of solitary waves and ascend with constant velocity and staying in shape. This regime can be further divided into 1a ($r < 20 \cdot \delta_c$), where the solid mass flux is negative, and 1b ($20 \cdot \delta_c \leq r < 36 \cdot \delta_c$), where the solid moves upwards with the melt. Waves in these regimes are very similar and differ only in the matrix flux.

In the solitary wave composed diapiric uprising regime (2) ($r \geq 36 \cdot \delta_c$), C_{dia} is larger than C_{solid} but, as the fluid melt is still able to move relatively to the solid matrix, solitary waves build up and the whole partially molten region will evolve into a swarm of them. The phase velocities of these waves are very small compared to the Stokes velocity of the perturbation and the whole swarm will rise as a diapir, whose buoyancy is still comparable to the buoyancy of the initial perturbation's.

A third regime can be reached by prohibiting the relative movement of fluid ($r = \infty \cdot \delta_c$), for which the compaction length has not to be sufficiently resolved. In this regime the initial perturbation will not disintegrate into solitary waves but rise as a well-formed partially molten diapir. In every other case where fluid is able to move w.r.t. the solid, at some point all diapirs will evolve into a swarm of solitary waves which can be infinitely small compared to the initial perturbation. However, this is expected to happen only after a long distance of diapiric rise. In cases where the size of solitary waves is comparable to the perturbation (e.g. regime (1)) this will occur sooner and in cases, where solitary waves are much smaller, later. Their observation is mostly limited by resolution.

4 Discussion

4.1. Application to nature

While in our models the perturbation size in terms of compaction lengths was systematically varied but kept constant within in each model, our results might also be applicable to natural cases in which the compaction length varies vertically. In the case of compaction length decreasing with ascent a porosity anomaly might start rising as a solitary wave but then at some point might enter the second regime where diapiric rise is dominant. If this boundary is sharp, the solitary wave might disintegrate into several

400 smaller solitary waves that rise diapiric as a swarm. If the boundary is a continuous transition the wave should slowly shrink and become slower. The melt left behind might also evolve into secondary solitary waves.

A decreasing compaction length could be accomplished by decreasing the matrix viscosity or the permeability, or by increasing the fluid viscosity. Decreasing matrix viscosity might be for example 405 explainable by local heterogeneities, temperature anomalies for example due to secondary convective overturns in the asthenosphere or by a vertical gradient of water content, which may be the result of melt segregation aided volatile enrichment at shallow depths in magmatic systems. This could lead to the propagation of magma-filled cracks (Rubin, 1995) as already pointed out in Connolly & Podladchikov (1998). The latter authors have looked at the effects of rheology on compaction-driven fluid flow and 410 came to similar results for an upward weakening scenario. The decrease of permeability due to decrease in background porosity might be an alternative explanation. In the hypothetical case of a porosity wave reaching the top of a magma chamber, the background porosity might decrease which would most certainly lead to focusing, because the compaction length will decrease, and eventually, when reaching melt free rocks, the solitary waves might be small enough and its amplitude might be high enough to 415 trigger the initiation of dykes.

While we propose that all partially molten diapirs which allow for two-phase flow will inevitably disintegrate into numerous solitary waves when two-phase flow is allowed, it doesn't mean that there are no classical diapirs in nature. Within regime (1) solitary waves are possible and most probably expected but the deeper we are in regime (2) the less expected is the disintegration because they need a 420 long time to build up. In nature compared to the time scale of diapiric rise, different from our models, they cannot rise for an infinite amount of time. The time needed to build up a solitary wave increases non-linearly with r (c.f. Fig. 3 1). For example, while for $r = 4.8 \cdot \delta_c$ a solitary wave is completely evolved after $t' = 0.02$, for $r = 48 \cdot \delta_c$ it needs until $t' = 0.4$, i.e. equivalent to the diapiric rise time necessary to ascend the distance approximately half the initial radii.

425 Our results show that large partially molten bodies with sizes of about $r > 20 \cdot \delta_c$ are expected to rise as diapirs but have the potential to split up into a number of solitary waves. Such sizes translate to > 2 km – 200 km for typical compaction length within the earth. If such swarms of solitary waves reach the base of the lithosphere each solitary wave may trigger a melt extraction and volcanic event. Given the size of the original diapir, its rising velocity and the number of solitary waves, we might speculate that 430 the episodicity of melt extraction may be related to the time-dependent arrival of the solitary waves. For example, assuming a compaction length of 100 m to 1 km, a 3D diapir with $r = 40 \cdot \delta_c = 40$ km would possibly split up into several hundred to several 100 thousand solitary waves each having a radius of order $4 \cdot \delta_c$. With a typical Stokes velocity of a 10 cm/a for the whole body it would release magmas from each solitary wave with a rate of order one per 1 ka to 1 per year. Such extraction rates are in good 435 agreement with observed eruption rates e.g. in Hawaii (e.g. Schmeling, 2006, and references therein).

4.2. Other issues

The introduced partition coefficients help to distinguish whether solitary wave or diapiric rise is dominant but cannot be solely consulted whether a solitary wave or a diapir can be expected. As the fluid velocity and flux is still very high in the waves center for diapiric dominant cases, small solitary waves will build up. However, the net mass flux is dominated by the large scale rising solid, and the formation time of small solitary waves might be long.

Nevertheless, we propose that all partially molten perturbations allowing for two-phase flow emerge into solitary waves, while those with batch melting rise as diapirs. While the minimum size of solitary waves in nature might be in some way limited by the grain size, in numerical models the minimum size is limited by the model's resolution. We restrict our models in this study to cases where the compaction length is at least resolved by 3 grid lengths dx (i.e. $\delta_c \geq 3 \cdot dx$) to get fairly resolved solitary waves, but they can be also observed for much worse resolved compaction lengths. The resolution test (Fig. 2) shows that, even though they are not solved decently, probable solitary waves can be observed for cases with $\delta_c = dx$. Smaller resolutions can show indications of solitary waves but should not be trusted as other tests (not shown here) with similar resolutions result in spurious channeling. For very poorly resolved compaction lengths no indications of solitary waves can be observed, and the partially molten perturbation ascends as a diapir. The deeper we are in regime 2, the more dominant are the dynamics of diapirism on a length scale of r compared to Darcy flow or solitary waves on the unresolved length scale of δ_c . Thus, two-phase flow, either Darcy flow or solitary waves, becomes negligible for $r \gg \delta_c$ and partially molten diapirs can be regarded as well resolved.

5 Conclusion

This work shows, that depending on the extent of a partially molten region within the earth, the resulting ascent of melt may not only occur by solitary waves or by diapirs, but by a composed mechanism, where a diapir splits up into numerous solitary waves. Their phase velocities might become so slow that the whole swarm will ascend as a diapir, just slowly elongating due to the main solitary wave having a higher amplitude and therefore higher phase velocity than the following ones. Depending on the ratio of the melt anomalies size to the compaction length, or rather the models length scale to compaction length ratio, we can classify the ascent behavior into three different regimes using mass flux and velocity of matrix and melt: (1) Solitary wave a and b, (2) solitary wave composite diapirism and (3) diapirism. In regime 1a the matrix sinks with respect to the rising melt, in 1b also the matrix rises, but very slowly. On first order these regimes can be explained by comparing Stokes velocity of the rising perturbation with the solitary waves phase velocity. If the solitary wave velocity is higher than the Stokes velocity a solitary wave will evolve and, if lower, diapirism is dominant, but still solitary waves will build up if the ascending time is long enough. The deeper we are in regime 2, the more time is needed to build up

470 solitary waves and the less likely it is that they will appear in nature. The third regime can be only reached if fluid is not allowed to move separately to the matrix.

Especially in the second regime numerical resolution plays an important role as the compaction length might be no longer resolved properly to allow for the emergence of solitary waves. Hence it should be generally important for two-phase flow models to inspect whether solitary waves are expected and if so, do they have a major influence on the conclusions made.

Code availability

The used finite difference code, FDCON, is available on request.

Author Contribution

Janik Dohmen wrote this article and carried out all models shown here. Harro Schmeling helped preparing this article and initialized this project.

References

Barcilon, V., & Lovera, O. M.: Solitary waves in magma dynamics. *Journal of Fluid Mechanics*, 204(1989), 121–133. <https://doi.org/10.1017/S0022112089001680>, 1989.

Bittner, D., & Schmeling, H.: Numerical modelling of melting processes and induced diapirism in the lower crust. *Geophysical Journal International*, 123(1), 59-70, 1995.

Connolly, J. A. D.: Devolatilization-generated fluid pressure and deformation-propagated fluid flow during prograde regional metamorphism. *Journal of Geophysical Research: Solid Earth*, 102(B8), 18149-18173, 1997.

Connolly, J. A. D., & Podladchikov, Y. Y.: Compaction-driven fluid flow in viscoelastic rock. *Geodinamica Acta*, 11(2–3), 55–84. <https://doi.org/10.1080/09853111.1998.11105311>, 1998.

Connolly, J. A. D., & Podladchikov, Y. Y.: A hydromechanical model for lower crustal fluid flow. In *Metasomatism and the chemical transformation of rock* (pp. 599-658). Springer, Berlin, Heidelberg, 2013.

Connolly, J. A. D., & Podladchikov, Y. Y.: An analytical solution for solitary porosity waves: Dynamic permeability and fluidization of nonlinear viscous and viscoplastic rock. *Geofluids*, 15(1–2), 269–292. <https://doi.org/10.1111/gfl.12110>, 2015.

Dohmen, J., Schmeling, H., & Kruse, J. P.: The effect of effective rock viscosity on 2-D magmatic porosity waves. *Solid Earth*, 10(6), 2103-2113, 2019.

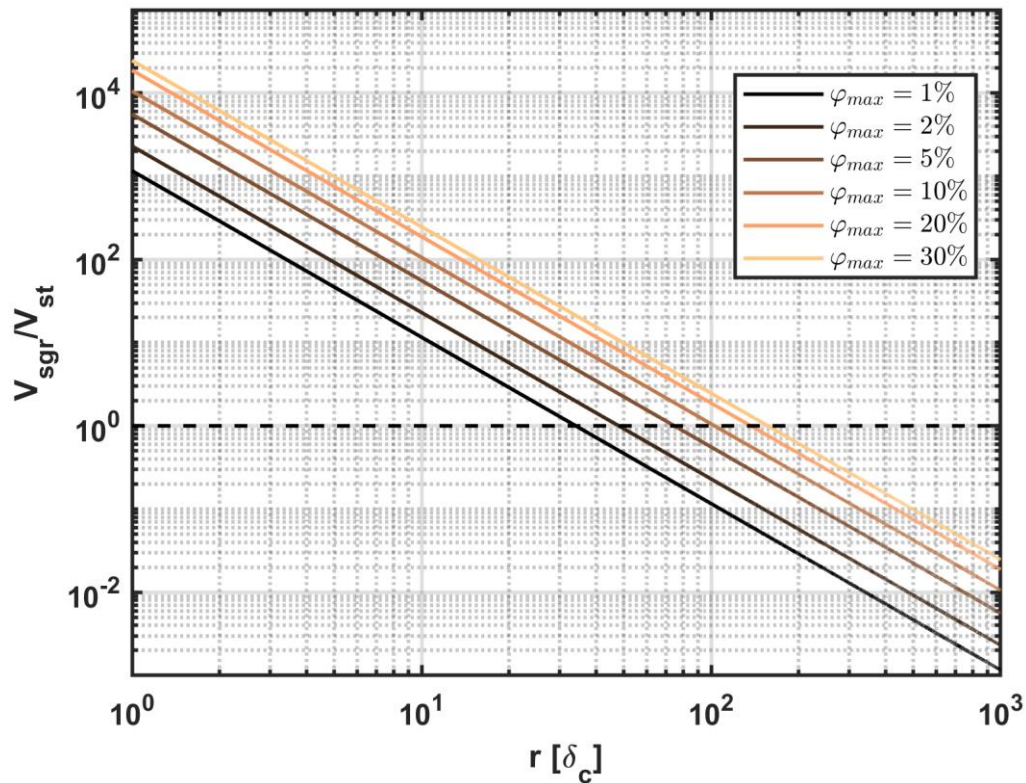
- 500 Golabek, G. J., Schmeling, H., & Tackley, P. J. (2008). Earth's core formation aided by flow
channelling instabilities induced by iron diapirs. *Earth and Planetary Science Letters*, 271(1-
4), 24-33.
- Griffiths, R. W.: The differing effects of compositional and thermal buoyancies on the evolution of
mantle diapirs. *Physics of the earth and planetary interiors*, 43(4), 261-273, 1986.
- Jordan, J. S., Hesse, M. A., & Rudge, J. F.: On mass transport in porosity waves. *Earth and Planetary*
505 *Science Letters*, 485, 65–78. <https://doi.org/10.1016/j.epsl.2017.12.024>, 2018.
- Keller, T., May, D. A., & Kaus, B. J.: Numerical modelling of magma dynamics coupled to tectonic
deformation of lithosphere and crust. *Geophysical Journal International*, 195(3), 1406-1442,
2013.
- McKenzie, D.: The generation and compaction of partially molten rock. *Journal of Petrology*, 25(3),
510 713–765. <https://doi.org/10.1093/petrology/25.3.713>, 1984.
- Omlin, S., Malvoisin, B., & Podladchikov, Y. Y.: Pore Fluid Extraction by Reactive Solitary Waves in
3-D. *Geophysical Research Letters*, 44(18), 9267–9275. <https://doi.org/10.1002/2017GL074293>,
2017.
- Popov, A. A., S.V. Sobolev: SLIM3D: A tool for three-dimensional thermomechanical modeling of
515 lithospheric deformation with elasto-visco-plastic rheology. *Phys. Earth Planet. Int.*, 171, 55 –
75, 2008.
- Räss, L., Duretz, T., & Podladchikov, Y. Y.: Resolving hydromechanical coupling in two and
three dimensions: Spontaneous channelling of porous fluids owing to decompaction
weakening. *Geophysical Journal International*, 218(3), 1591–1616.
520 <https://doi.org/10.1093/gji/ggz239>, 2019.
- Richard, G. C., Kanjilal, S., & Schmeling, H. (2012). Solitary-waves in geophysical two-phase viscous
media: A semi-analytical solution. *Physics of the Earth and Planetary Interiors*, 198–199, 61–
66. <https://doi.org/10.1016/j.pepi.2012.03.001>
- Richardson, C. N.: Melt flow in a variable viscosity matrix. *Geophysical Research Letters*, 25(7),
525 1099-1102, 1998.
- Rubin, A. M.: Propagation of magma-filled cracks. *Annual Review of Earth and Planetary Sciences*,
287–336, 1995.
- Schmeling, H.: Partial melting and melt segregation in a convecting mantle. In *Physics and Chemistry
of Partially Molten Rocks*. Springer, 2000.

- 530 Schmeling, H., Marquart, G., Weinberg, R., & Wallner, H.: Modelling melting and melt segregation by two-phase flow: New insights into the dynamics of magmatic systems in the continental crust. *Geophysical Journal International*, 217(1), 422–450. <https://doi.org/10.1093/gji/ggz029>, 2019.
- Scott, D. R.: The competition between percolation and circulation in a deformable porous medium. *Journal Of Geophysical Research*, 93(B6), 6451–6462.
535 <https://doi.org/10.1029/JB093iB06p06451>, 1988
- Scott, D. R., & Stevenson, D. J.: Magma solitons. *Geophysical Research Letters*, 11(11), 1161–1164, 1984.
- Simpson, G., & Spiegelman, M.: Solitary wave benchmarks in magma dynamics. *Journal of Scientific Computing*, 49(3), 268–290. <https://doi.org/10.1007/s10915-011-9461-y>, 2011.
- 540 Spiegelman, M.: Physics of Melt Extraction: Theory, Implications and Applications. *Philosophical Transactions of the Royal Society A: Mathematical, Physical and Engineering Sciences*, 342(1663), 23–41. <https://doi.org/10.1098/rsta.1993.0002>, 1993.
- Spiegelman, M.: Flow in deformable porous media. Part 2 Numerical analysis - the relationship between shock waves and solitary waves. *J. Fluid Mech.*, 247, 39–63.
545 <https://doi.org/10.1017/S0022112093000370>, 1993.
- Spiegelman, M., & McKenzie, D.: Simple 2-D models for melt extraction at mid-ocean ridges and island arcs. *Earth and Planetary Science Letters*, 83(1-4), 137-152, 1987.
- Šrámek, O., Ricard, Y., & Dubuffet, F. : A multiphase model of core formation. *Geophysical Journal International*, 181(1), 198-220, 2010.
- 550 Stevenson, D. J.: Spontaneous small-scale melt segregation in partial melts undergoing deformation. *Geophysical Research Letters*, 16(9), 1067-1070, 1989.
- Slezkin, A.: Dynamics of viscous incompressible fluid. Gostekhizdat, Moscow (in Russian), 1955.
- Turcotte, D. L., & Schubert, G.,. *Geodynamics*. Cambridge university press., 1982.
- Watson, S., & Spiegelman, M.: Geochemical Effects of Magmatic Solitary Waves—I. Numerical
555 Results. *Geophysical Journal International*, 117(2), 284–295. <https://doi.org/10.1111/j.1365-246X.1994.tb03932.x>, 1994.
- Wiggins, C., & Spiegelman, M.: Magma migration and magmatic solitary waves in 3D. *Geophysical Research Letters*, 22(10), 1289–1292. <https://doi.org/10.1029/95GL00269>, 1995.

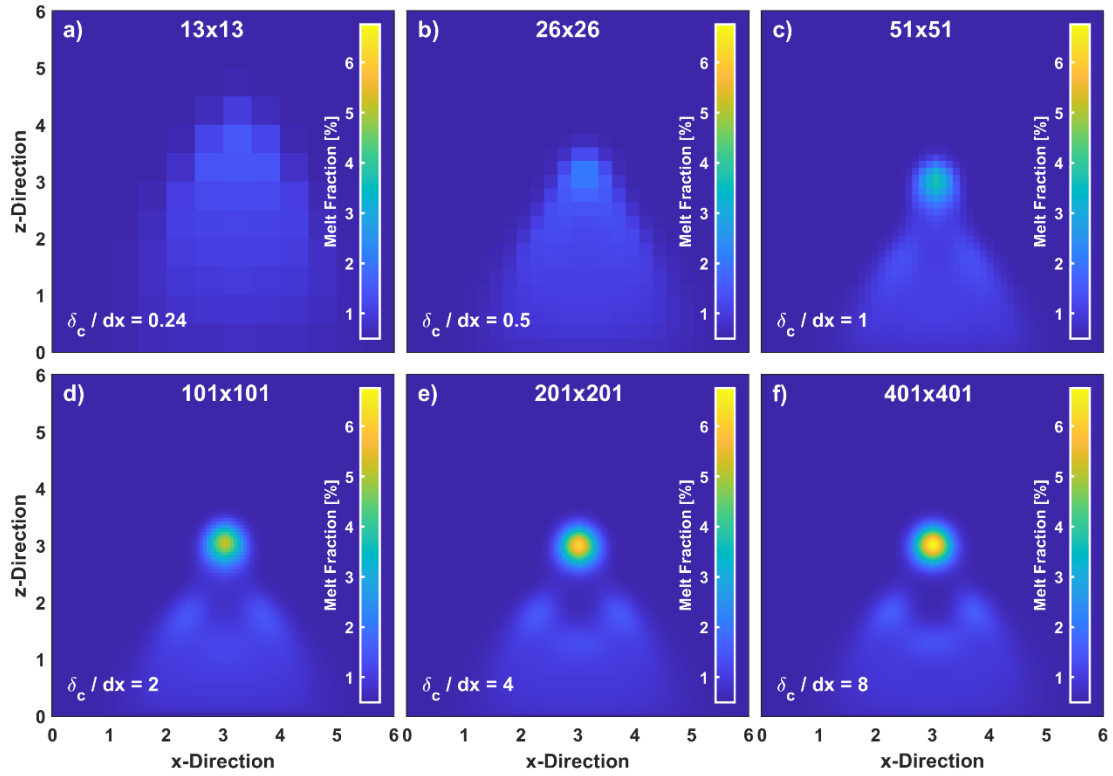
Collins, W. J.: Polydiapirism of the Archean Mount Edgar Batholith, Pilbara Block, Western Australia. *Precambrian Research*, 43(1-2), 41-62, 1989.

560

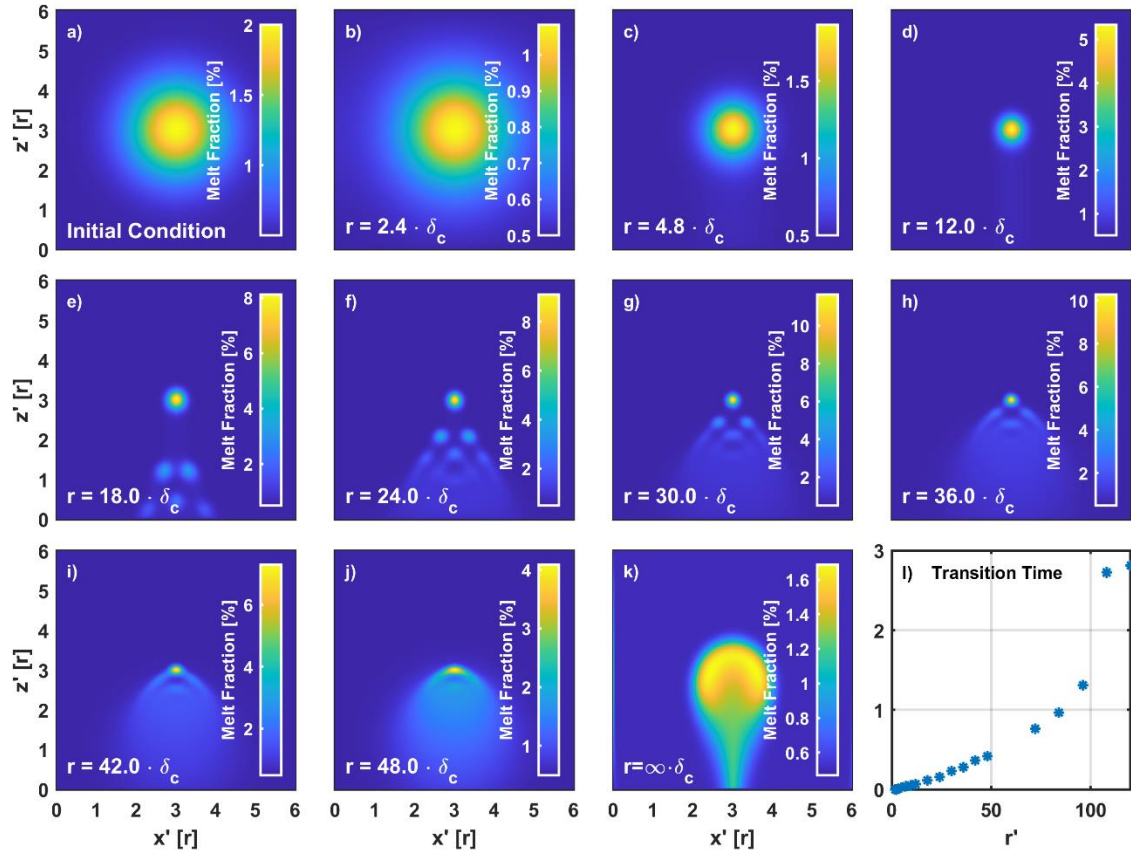
Yarushina, V. M., Podladchikov, Y. Y., & Connolly, J. A. D.: (De)compaction waves in porous viscoelastoplastic media: Solitary porosity waves. *Journal of Geophysical Research: Solid Earth*, 1–20. <https://doi.org/10.1002/2014JB011260>. Received, 2015.



565 **Fig. 1:** The segregation to Stokes velocity ratio, following equation (21), is given as a function of initial perturbation radius r in terms of compaction length δ_c . Each colored line refers to different values of perturbation amplitude φ_{max} , given in the legend.



570 **Fig. 2:** All six figures show a model with an initial perturbation radius of 12 times the compaction length but with different resolutions: a) 13x13 b) 26x26 c) 51x51 d) 101x101, e) 201x201, f) 401x401. In the lower left corner in each figure the size of the compaction length in terms of grid length is given.



575 **Fig. 3:** a) Shows the initial condition of our models, which looks equal for all cases. Only the compaction length is changed. b-j) give the resulting melt fraction distribution after $t' = 0.2$ for different length scale ratios between 2.4 and 48. k) shows a classical diapir, referring to a compaction length of zero, at $t' = 9$. l) shows the transition time of models with length scale ratios between 1.8 and 120. The transition time gives the time after which the main wave has reached a
580 solitary wave status.

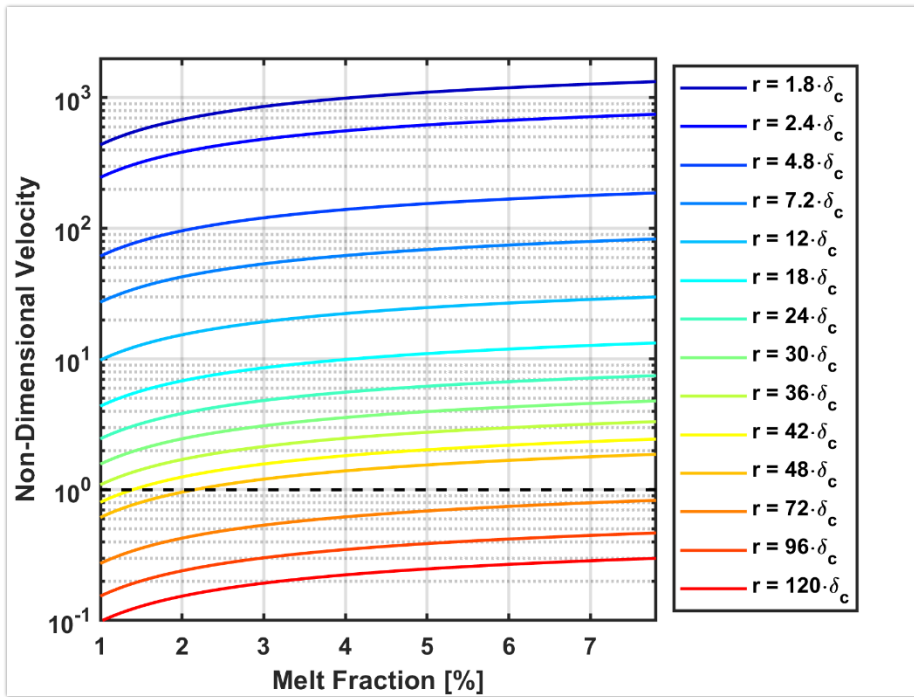


Fig. 4: The dashed line marks the velocity of the Stokes sphere ($v' = 1$). The colored lines show the velocity of a 2D solitary wave, calculated semi-analytically by Simpson & Spiegelman (2011), in our non-dimensionalization, based on the radii shown in the legend.

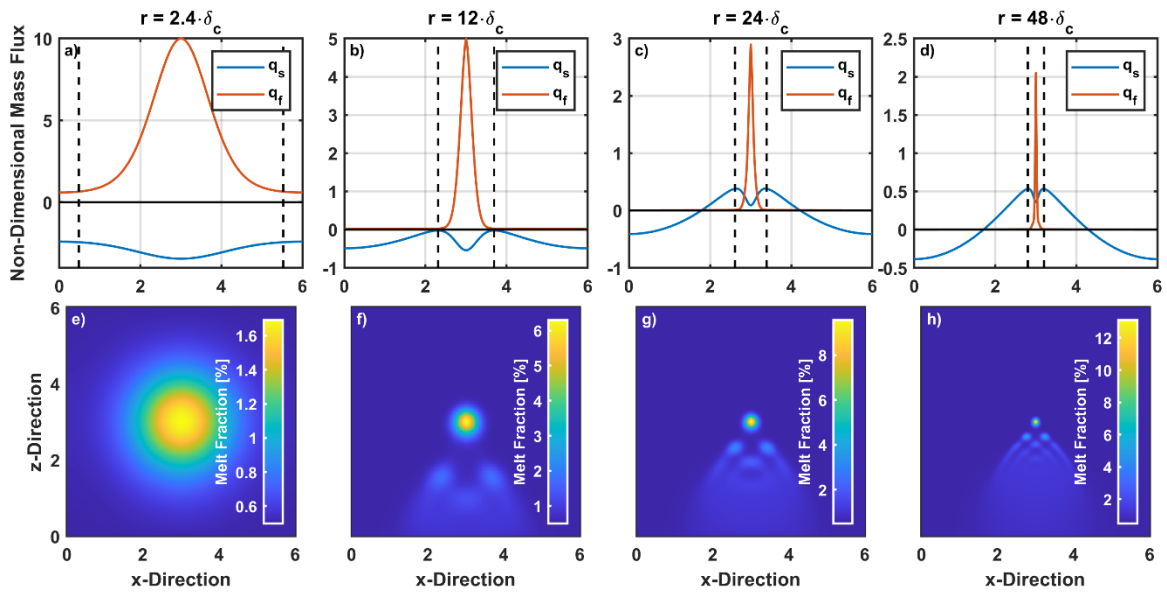


Fig. 5: The upper row gives the solid and fluid mass fluxes of a horizontal line cutting through the maximum melt fraction at timesteps where the main wave has just reached the status of a solitary wave. These timesteps are $t' = 0.02; 0.068; 0.155; 0.416$, respectively from left to right. The bottom row gives the corresponding melt porosity fields. All quantities shown are non-dimensional.

585

590

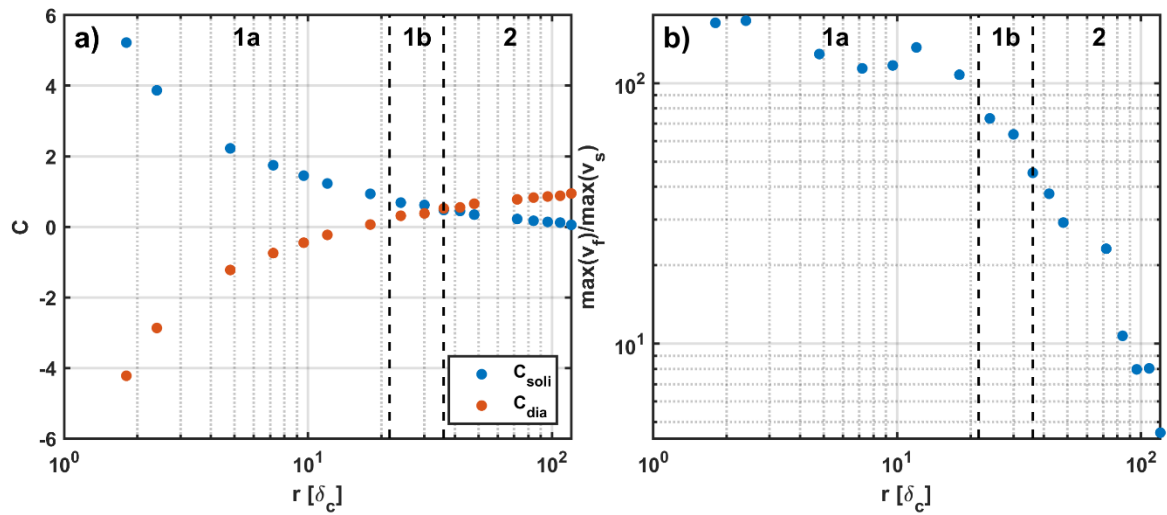


Fig. 6: a) The graph shows the solitary wave (blue) and diapir (red) partition coefficients for several initial perturbation radii. The dashed lines describe the borders of the regimes. Figure b) shows the ratio of maximum fluid velocity to maximum absolute solid velocity in the whole model.